

# Larmor radius effect on the control of chaotic transport in tokamaks

L.A. Osorio-Quiroga,<sup>1, a)</sup> M.Roberto,<sup>2, b)</sup> R.L. Viana,<sup>3</sup> Y. Elskens,<sup>4</sup> and I.L. Caldas<sup>1</sup>

<sup>1)</sup> *University of São Paulo, Institute of Physics, 05508-090 São Paulo, SP, Brazil*

<sup>2)</sup> *Aeronautics Institute of Technology, Physics Department, 12228-900 São José dos Campos, SP, Brazil*

<sup>3)</sup> *Federal University of Paraná, Physics Department, 81531-990 Curitiba, PR, Brazil*

<sup>4)</sup> *Aix-Marseille Université, UMR 7345 CNRS, PIIM, 13397 Marseille, France*

(Dated: 24 July 2024)

We introduce a second-order gyro-averaged extension to a guiding-center transport model for test particles subject to an  $\mathbf{E} \times \mathbf{B}$  drift in a tokamak. Using this approximation, we numerically investigate the influence of finite Larmor radius effects on the chaotic transport and the formation of transport barriers. For non-monotonic plasma profiles, we show that the twist condition of the system is violated along a curve, usually called shearless transport barrier, which, under non-equilibrium conditions, exhibits significant resilience to destruction, thereby inhibiting chaotic transport. We analyze bifurcation diagrams of the shearless barriers and escape rates to explore the impact of the Larmor radius on controlling chaotic transport while varying the amplitude of electrostatic perturbations. Our findings show that increasing the Larmor radius enhances the robustness of transport barriers, as a larger electrostatic perturbation amplitude is required to disrupt them. Additionally, even in the absence of transport barriers, we observe a decrease in chaotic transport with an increase in the Larmor radius.

## I. INTRODUCTION

It is well-known that the transverse transport coefficients of tokamak plasmas, predicted by neo-classical theory, are much smaller than the experimental results available by one order of magnitude or more, the difference between them is usually called anomalous transport<sup>1</sup>. The scenarios projected for a future operation of a tokamak-based thermonuclear fusion reactor depend crucially on the control of anomalous transport of the confined plasma, which is expected to yield a substantial reduction in the loss of particles and heat<sup>2</sup>. It is generally believed that turbulence driven by micro-instabilities causes anomalous transport, although it is still a matter of some controversy about how important turbulence really is, since neo-classical transport is always present<sup>3,4</sup>.

While there is no complete theory of turbulence-driven anomalous transport, it has been proved useful to model the net effect of turbulence by using a non-diffusive description<sup>5-7</sup>. One of the aspects of the latter is the existence of internal transport barriers, responsible for reducing radial particle transport inside the plasma, and which are associated with rational magnetic surfaces, and chaotic regions of the magnetic field<sup>8,9</sup>.

In this work, we will consider a special type of internal transport barrier, called shearless transport barrier (STB), which can occur for non-monotonic configurations of the plasma profiles, for example, for the safety factor, the radial electric field, and the toroidal plasma velocity<sup>10</sup>. Such profiles may lead to non-twist behavior for which the twist condition of the system is violated on a given curve, i.e., the STB, where the angular frequency

of the motion has an extremum<sup>11</sup>. From a dynamical point of view, non-twist systems have an unusual behavior because standard results, such as KAM theory, Chirikov stochasticity criterion, etc. may not be valid<sup>12</sup>. The degeneracy of the system allows the formation of twin (dimerized) islands which, as a non-linearity parameter is varied, do not overlap and break down as they do in twist systems. In non-twist systems, twin islands experience a kind of reconnection and a shearless curve prevents the formation of a large chaotic region<sup>13,14</sup>. The shearless curve acts as a robust internal transport barrier since it is resilient under variations of the non-linearity parameter, i.e., a strong perturbation is required to destroy it<sup>15,16</sup>.

Recent numerical investigations of STBs rely on simple transport models based on an  $\mathbf{E} \times \mathbf{B}$  drift guiding-center motion of test particles<sup>17,18</sup>. By “test particles” we mean charged particles that have a motion determined by the combined action of electric and magnetic fields, which are produced by external sources and the plasma itself, but whose motion does not affect the fields. Hence, the test particle description is more appropriate to describe the transport of impurities present in the plasma, like ions produced by the plasma-wall interaction<sup>19</sup>.

This description has been explored in recent works that have dealt with different features of chaotic transport of impurities when STBs are present<sup>19-21</sup>. In most of these works, we assume that the Larmor radius is too small to play a significant role in the dynamics. However, this assumption may not be valid if the electric field has spatial variations in very small scales or the particles are fast, e.g., alpha particles in burning plasmas<sup>22,23</sup>. In such cases, we have to take into account finite Larmor radius (FLR) effects in the expression for the gyro-averaged drift velocity<sup>24,25</sup>.

In this work, we aim to characterize the influence of the FLR on the appearance of STBs and the chaotic transport. The drift motion of impurities is described

<sup>a)</sup>Electronic mail: losorio@usp.br

<sup>b)</sup>In memory of Marisa Roberto, an invaluable collaborator whose significant contributions to our work will be greatly missed.

using the transport model from Ref. 18, with a suitable second-order gyro-averaged extension. We consider a non-monotonic radial equilibrium electric field profile and an electrostatic perturbation regarded as the superposition of coherent harmonic waves traveling in the poloidal and toroidal directions. Additionally, monotonic profiles for the safety factor and the toroidal velocity are assumed. Since the applied model has a Hamiltonian structure, the phase space flow generated by solving the equations of motion is area-preserving in an adequate Poincaré surface of section. Accordingly, this is an area-preserving map that violates the twist property at the radial position of a shearless curve.

The Larmor radius and the electrostatic perturbation amplitude of one harmonic mode are taken as control parameters to be varied. We introduced suitable quantifiers for the chaotic transport like the transmissivity of the barrier and the transport current, associated with the probability of a given orbit to escape and the escape rate, respectively. Bifurcation diagrams of the STB as a function of the control parameters are obtained.

Then, we show that by increasing the FLR effect the chaotic transport is reduced, and the transport barriers are enhanced. In agreement with our results, other works have shown that the averaging effect caused by the large Larmor radius in electrostatic turbulence is that of suppressing the stochastic diffusion<sup>22</sup>. In the presence of STBs, this is driven by a super-diffusive behavior transverse to the transport direction<sup>26</sup>. Furthermore, models based on discrete gyro-averaged area-preserving maps have found that the probability for a particle remaining trapped in a drift-wave resonance increases when the Larmor radius increases, improving the particle confinement<sup>25,27</sup>. In particular, the inclusion of the FLR effect changes the properties of transport since it leads to chaos suppression<sup>25,28</sup>.

This paper is organized as follows: Section II describes the drift wave transport model with finite Larmor radius effect. Section III presents a dynamical analysis of the phase space of our numerical map, emphasizing the computation of the rotation number and presenting bifurcation diagrams for the STB as a function of the perturbation amplitude for different Larmor radii. The diagnostics used to characterize the reduction of chaotic transport are introduced in Section IV, as well as a comprehensive analysis of the corresponding parameter plane. Our conclusions are left to Section V.

## II. DRIFT WAVE TRANSPORT MODEL

Let us consider an individual test particle that is immersed in a large aspect-ratio tokamak plasma, i.e.,  $1/\varepsilon = R/a \gg 1$ , with  $R$  and  $a$  the major and minor radii of the plasma column, respectively. The particle's guiding center is moving along the lines of the magnetic field,  $\mathbf{B}(\mathbf{x})$ , with velocity  $\mathbf{v}_{\parallel}(\mathbf{x})$  and drifted by the gyro-averaged velocity  $\mathbf{v}_{\mathbf{E}}(t, \mathbf{x})$ , evaluated at the

guiding center, so that

$$\frac{d\mathbf{x}}{dt} = \mathbf{v}_{\parallel} + \mathbf{v}_{\mathbf{E}}, \quad (1a)$$

$$\mathbf{v}_{\mathbf{E}} = \left( \mathbf{E} + \frac{1}{4}\rho^2\nabla_{\perp}^2\mathbf{E} \right) \times \frac{\mathbf{B}}{B^2}, \quad (1b)$$

where  $\rho$  is the Larmor radius,  $\mathbf{E}(t, \mathbf{x})$  is the electric field and  $\nabla_{\perp}^2$  is the Laplacian taken on the perpendicular plane to  $\mathbf{B}$ .

This gyro-averaged drift velocity results from the averaging method presented in Ref. 29, taking up to second-order space-varying electric field contributions. This is a usual approximation that only considers the influence of a non-uniform electric field, and plays a fundamental role in describing transport in the presence of fast particles, such as alpha particles in burning plasmas<sup>23,30</sup>.

Although other drift velocities could be considered to evaluate the guiding center orbit due to the finite Larmor radius (FLR) effect, for simplicity, we say the particle has only the drift contribution of  $\mathbf{v}_{\mathbf{E}}$ . This approximation is valid under certain assumptions. Firstly, the geometrical limit  $\varepsilon \ll 1$  significantly reduces the impact of the magnetic field lines curvature. Also, we assume small gradients of the magnetic field, which cause the  $\mathbf{B} \times \nabla B$  drift. Hence, we consider a magnetic field such that

$$\mathbf{B}(r) = B_{\theta}(r)\hat{e}_{\theta} + B_{\varphi}(r)\hat{e}_{\varphi}, \quad (2)$$

with  $B \approx B_{\varphi} \gg B_{\theta}$  and  $B \approx B_0$ , where  $B_0$  is constant; and where  $r$ ,  $\theta$  and  $\varphi$  are the radial, poloidal and toroidal coordinates of the toroidal system, respectively.

Furthermore, let us consider that  $\nabla \times \mathbf{E} = \mathbf{0}$ . In the equilibrium,  $\mathbf{E}_{\parallel} = \mathbf{0}$  and the electric field is described fully by the radial equilibrium component  $E_r(r)\hat{e}_r$ . For the non-equilibrium scenario, we add a perturbation via the electrostatic potential  $\tilde{\phi}(t, \mathbf{x})$ . Therefore

$$\mathbf{E}(t, \mathbf{x}) = E_r(r)\hat{e}_r - \nabla\tilde{\phi}(t, \mathbf{x}), \quad (3a)$$

$$\tilde{\phi}(t, \theta, \varphi) = \sum_n \phi_n \cos(M\theta - L\varphi - n\omega_0 t + \alpha), \quad (3b)$$

where, to simplify the model, we have adopted the perturbative part as a superposition of coherent harmonic waves traveling in the poloidal and toroidal directions. By doing this, we reduce the original system, equations (1a), to a 1.5-degrees-of-freedom dynamical system and obtain a symplectic map, as we show further in this section. So, for the time-dependent perturbation in equation (3b), where  $M$  and  $L$  are its dominant wave numbers,  $\phi_n$  the wave amplitude of each mode,  $\alpha$  a constant phase, and  $\omega_0$  its fundamental angular frequency, we can neglect the polarization drift as long as

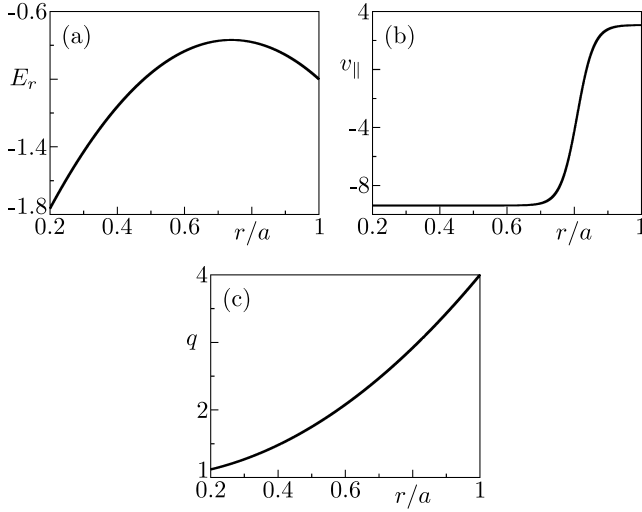


FIG. 1. Dimensionless plasma profiles, mainly, (a) the radial electric field,  $E_r(r)$ , (b) the parallel velocity,  $v_{\parallel}(r)$ , and (c) the safety factor,  $q(r)$ .

$\omega_g \gg \omega_0$ , where  $\omega_g$  is the cyclotron angular frequency, or gyro-frequency, of the particle.

Additionally, since  $\mathbf{B}$  is essentially toroidal, we only look at the Laplacian on the  $(r, \theta)$  plane. Then, by introducing two new variables, namely the action,  $I$ , and the angle,  $\psi$ , defined as

$$I = \left(\frac{r}{a}\right)^2, \quad (4a)$$

$$\psi = M\theta - L\varphi, \quad (4b)$$

and performing an adimensionalization by using the characteristic scales  $a$ ,  $E_a = |E_r(I=1)|$  and  $B_0$ , according to relations

$$\begin{aligned} E'_r &= \frac{E_r}{E_a}, & \phi'_n &= \frac{\phi_n}{aE_a}, & v'_{\parallel} &= \frac{B_0}{E_a}v_{\parallel}, & t' &= \frac{E_a}{aB_0}t, \\ \omega'_0 &= \frac{aB_0}{E_a}\omega_0, & \rho' &= \frac{\rho}{a}, \end{aligned} \quad (5)$$

the equations of motion (1a) simplify into the 1.5-degrees-of-freedom dynamical system

$$\frac{dI}{dt'} = -f(I) \frac{\partial \tilde{\phi}'(t', \psi)}{\partial \psi}, \quad (6a)$$

$$\frac{d\psi}{dt'} = g(I) + \frac{df(I)}{dI} \tilde{\phi}'(t', \psi), \quad (6b)$$

where  $f$  and  $g$  are functions of  $I$ , and  $g$  is called the twist function of the system. This function is important in the KAM theorem, as the twist condition (non-degeneracy)

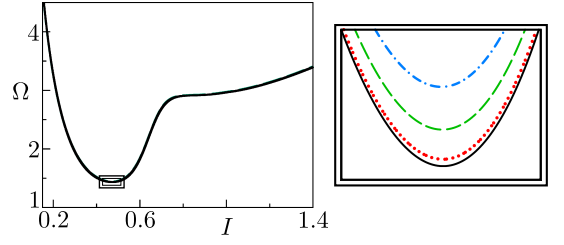


FIG. 2. Rotation number profile for the integrable case,  $H_1 = 0$ . The black (solid) curve corresponds to the massless approximation,  $\rho = 0.0$ , the red (dotted) one to  $\rho = 1.637 \times 10^{-2}$ , the green (dashed) one to  $\rho = 3.770 \times 10^{-2}$ , and the blue (dashed-dotted) one to  $\rho = 5.556 \times 10^{-2}$ .

$dg/dI \neq 0$  for all  $I$  ensures the robustness of KAM tori under perturbations<sup>31</sup>. Thus, a challenging dynamics, related to chaotic transport, occurs near the shearless curve, where  $dg/dI = 0$ , i.e., where the twist condition is broken<sup>32</sup>. In our model, the functions  $f$  and  $g$ , dropping the prime notation henceforth, correspond to

$$f(I) = 2M \left(1 - \frac{\rho^2 M^2}{4I}\right), \quad (7a)$$

$$g(I) = \varepsilon v_{\parallel}(I) \frac{M - Lq(I)}{q(I)} - \frac{M}{\sqrt{I}} (1 + \rho^2 \Delta) E_r(I), \quad (7b)$$

where  $\Delta = d/dI (I d/dI) - 1/(4I)$  is an operator which we introduce here and  $q(I) = \varepsilon \sqrt{I} B_{\varphi}/B_{\theta}$  is the safety factor profile.

Notice that, since  $\partial \dot{I}/\partial I + \partial \dot{\psi}/\partial \psi = 0$ , where the dot notation is the total time derivative, there is a Hamiltonian function,  $H(t, \psi, I)$ , such that

$$\dot{\psi} = \frac{\partial H}{\partial I}, \quad \dot{I} = -\frac{\partial H}{\partial \psi}, \quad (8)$$

which can be decomposed into an integrable,  $H_0(I)$ , and a perturbative part,  $H_1(t, \psi, I)$ ,

$$H(t, \psi, I) = H_0(I) + H_1(t, \psi, I), \quad (9)$$

where

$$H_0(I) = \int^I g(I') dI', \quad (10a)$$

$$H_1(t, \psi, I) = f(I) \tilde{\phi}(t, \psi). \quad (10b)$$

Thus, when  $H_1 = 0$ , i.e., when  $\phi_n = 0$  for all modes,  $I$  remains constant, and the guiding center orbit traces a helix of constant radius along a curve on the same equilibrium magnetic surface. On the other hand, when

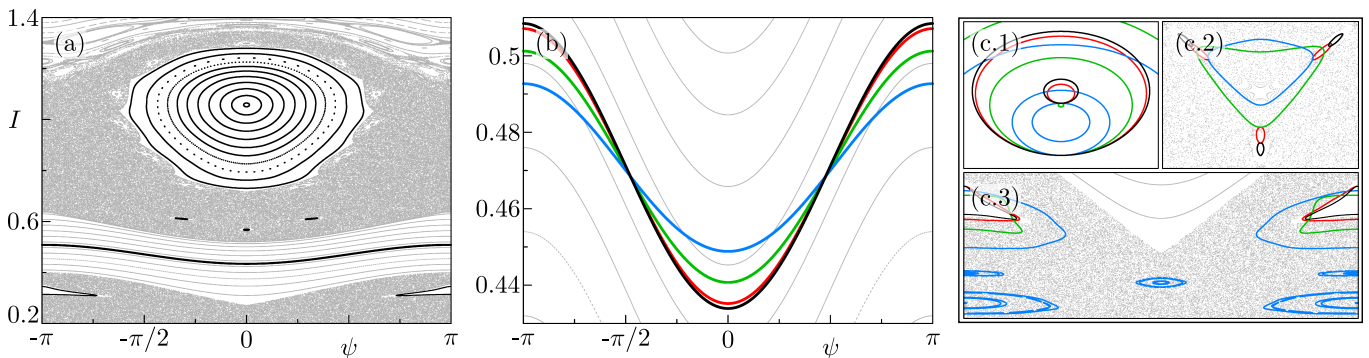


FIG. 3. Phase space for  $\phi_1 = 0.0$ . In gray and black colors, we show chaotic and quasi-periodic orbits for the massless case,  $\rho = 0.0$ . Red, green, and blue colors correspond to orbits for  $\rho = 1.637 \times 10^{-2}$ ,  $\rho = 3.770 \times 10^{-2}$  and  $\rho = 5.556 \times 10^{-2}$ , respectively. Panel (a) shows only the Poincaré section for  $\rho = 0.0$ ; meanwhile, panels (b) and (c) are magnifications of the shearless curve and the main islands, respectively, including the FLR effect. Specifically, in panel (c), we show magnifications around the black-colored islands in panel (a), ordering them from the top to the bottom.

$H_1 \neq 0$ , the integrability of the system is broken, leading to chaotic behavior and chaotic transport.

In the limit when  $\rho = 0$ , the dynamical system (6) reduces to the same equations introduced in Ref. 18. For these it has been shown that non-monotonic profiles of  $E_r(I)$ ,  $q(I)$  and  $v_{\parallel}(I)$  can lead to a non-twist behavior,  $dg/dI = 0$ , and the emergence of a non-twist barrier, addressed in the next section, that reduces the chaotic transport<sup>20,33–35</sup>.

However, we must be careful because the massless approximation is violated for cases when particles are fast, e.g., alpha particles, or even if we study impurity transport since the impurity temperature can be equivalent to the plasma's<sup>36</sup>. In those cases,  $\rho \approx 0$  is not valid anymore.

Therefore, we aim to investigate the influence that the FLR effect has on the onset of such barriers and also on chaotic transport. We consider for this a non-monotonic radial equilibrium electric field profile, and monotonic profiles for the safety factor and the parallel velocity.

Finally, although in this paper we only discuss the presented model in its ordinary differential form (6), we would like to show that an analytical symplectic map can be obtained and that it also represents an interesting topic, mainly, for studying the influence of the FLR effect and the plasma profiles on the chaotic transport. So, basically, on using the Fourier series representation of the Dirac delta function,  $\phi_n = \phi_0$  and  $\lambda(\psi) = \phi_0 \cos(\psi + \alpha)$ , the equations of motion (6) can be written as

$$\dot{I} = -2\pi f(I) \frac{d\lambda(\psi)}{d\psi} \sum_{n=-\infty}^{+\infty} \delta(\omega_0 t - 2\pi n), \quad (11a)$$

$$\dot{\psi} = g(I) + 2\pi \frac{df(I)}{dI} \lambda(\psi) \sum_{n=-\infty}^{+\infty} \delta(\omega_0 t - 2\pi n). \quad (11b)$$

Then, let us define  $I_n = I(t_n^-)$  and  $\psi_n = \psi(t_n^-)$ , with

$t_n^- = nT - \epsilon$ ,  $T = 2\pi/\omega_0$  and  $\epsilon \rightarrow 0^+$ . Integrating over one jump  $(t_n^-, t_{n+1}^-)$ , we obtain the discrete model

$$I_{n+1} = I_n - T f(I_{n+1}) \left. \frac{d\lambda(\psi)}{d\psi} \right|_{\psi_n}, \quad (12a)$$

$$\psi_{n+1} = \psi_n + T g(I_{n+1}) + T \left. \frac{df(I)}{dI} \right|_{I_{n+1}} \lambda(\psi_n), \quad (12b)$$

where the implicit form on  $I_{n+1}$  ensures the area-preserving nature of the map. Discrete models are useful because they reproduce the characteristic features of their differential counterparts and reduce the computational cost. For these reasons, we strongly encourage researchers to explore the map described by (12), as it promises valuable insights and advancements in the field.

### III. INFLUENCE OF THE FLR ON SHEARLESS TRANSPORT BARRIERS

Non-twist behavior is found in many physical problems, particularly in plasmas and fluid dynamics<sup>11,37–40</sup>. Systems exhibiting that behavior present resilient barriers that inhibit chaotic transport<sup>12</sup>, also known as shearless transport barriers (STBs), and feature a characteristic dynamics since the KAM theorem is not applicable due to the degeneracy of the system itself<sup>41</sup>.

Such barriers and the neighboring KAM curves, composing the non-twist barrier, are expected to be the latest invariant curves to be destroyed and also the easiest to restore<sup>42</sup>. Moreover, after the breakup, the remnant of the non-twist barrier, often accompanied by sticky behavior, acts as a partial barrier to transport<sup>15</sup>. So, the control of the chaotic transport is generally reduced to knowing whether the STB exists, how robust it is, and even more, how resilient and effective the partial barriers are. Specifically, in this section, we are interested in

evaluating the influence of the FLR on the onset of STBs as control parameters vary.

For that, let us establish the numerical map  $\mathbf{z}_{j+1} = M(\mathbf{z}_j)$ , where  $\mathbf{z}_j = (\psi_j, I_j) = (\psi(t_j), I(t_j))$ ,  $j \in \mathbb{N}$  and  $M$  is a numerical integration of the dynamical system (6) that evolves the orbit, given the initial condition  $\mathbf{z}_0$  at time  $t_0 = 0$ , from  $t_j$  to  $t_j + T$ , with  $T = 2\pi/\omega_0$ . By doing that, we construct stroboscopic Poincaré sections of the periodic, quasi-periodic, or chaotic guiding-center orbits. The results presented in this work were obtained using the numerical integrator Runge-Kutta-Dormand-Prince of 8(7) order<sup>43</sup>.

So, to find a STB, we calculate the rotation number

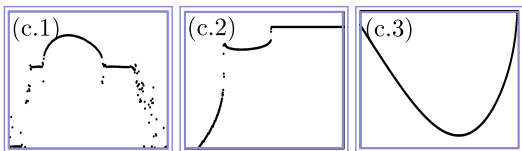
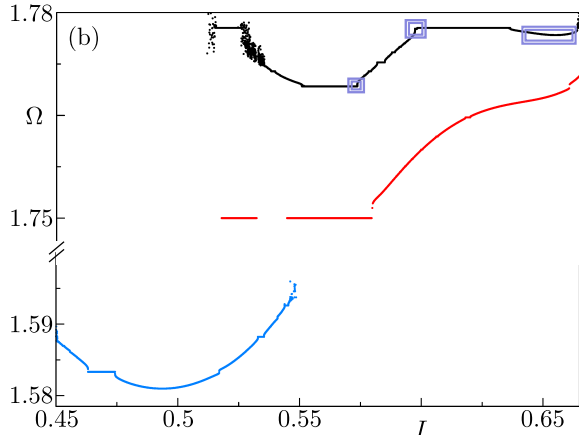
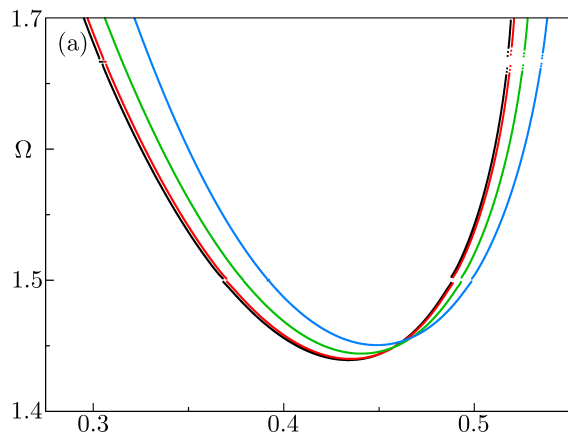


FIG. 4. Rotation number profiles for  $H_1 \neq 0$ , (a)  $\phi_1 = 0.0$ , and (b)  $\phi_1 = 2.283 \times 10^{-2}$ . Black, red, green, and blue colors correspond to  $\rho = 0.0$ ,  $\rho = 1.637 \times 10^{-2}$ ,  $\rho = 3.770 \times 10^{-2}$  and  $\rho = 5.556 \times 10^{-2}$ , respectively. For the black-colored profile in panel (b), we present in panel (c) magnifications around three different extrema where shearless curves can be identified. Specifically, (c.1) is near  $I = 0.57$ , (c.2) near  $I = 0.60$  and (c.3) near  $I = 0.65$ .

profile  $\Omega(\mathbf{z})$  and identify whether it has an extreme value  $(\partial\Omega/\partial I)_{\mathbf{z}_{\text{STB}}} = 0$ , from which a shearless orbit, corresponding to the barrier, can be generated by using  $\mathbf{z}_{\text{STB}}$  as the initial condition. The rotation number of an orbit is essentially the average angular displacement experienced by the orbit, so it will be rational if the orbit is periodic and irrational if it is quasi-periodic. To calculate it, we use the method proposed in Ref. 44, by which we obtained a reliable convergence of  $\Omega$  with less iterations. Therefore,

$$\Omega = \frac{1}{2\pi} \sum_{j=0}^{K-1} \hat{s}_{j,K} \Pi(M(\mathbf{z}_j) - \mathbf{z}_j), \quad (13a)$$

$$\hat{s}_{j,K} = \frac{s(j/K)}{\sum_{j=0}^{K-1} s(j/K)}, \quad (13b)$$

$$s(x) = \begin{cases} \exp\left(\frac{-1}{x(1-x)}\right), & \text{for } x \in (0, 1) \\ 0, & \text{for } x \notin (0, 1), \end{cases} \quad (13c)$$

where  $\Pi$  is a suitable angular projection, that for our particular problem can be taken as  $\Pi(\mathbf{z}_j) = \psi_j$ . Also, notice we are performing a normalization by  $2\pi$ .

For the integrable case,  $H_1 = 0$ , it is easy to show the rotation number of the  $T$ -period stroboscopic map does not depend on the initial angle  $\psi_0$  and is equal to  $\Omega = g(I)/\omega_0$ . In consequence, according to the configuration of the profiles  $E_r(I)$ ,  $v_{\parallel}(I)$  and  $q(I)$ , see equation (7b), the twist condition can be violated and, therefore, STBs appear at the zero-derivative points of  $g(I)$ .

Specifically, we take into account the plasma profiles and parameters for the tokamak TCABR<sup>45-47</sup>, for which the minor and major radii are  $a = 0.18$  m and  $R = 0.61$  m, respectively, and the toroidal magnetic field is  $B_0 = 1.20$  T. The plasma profiles are taken in the form

$$E_r(r) = E_0 + E_1 \left(\frac{r}{a}\right) + E_2 \left(\frac{r}{a}\right)^2, \quad (14a)$$

$$v_{\parallel}(r) = v_0 + v_1 \tanh\left[\beta_1 \left(\frac{r}{a}\right) + \beta_0\right], \quad (14b)$$

$$q(r) = \begin{cases} q_0 + (q_a - q_0) \left(\frac{r}{a}\right)^2, & \text{for } r \leq a \\ q_a \left(\frac{r}{a}\right)^2, & \text{for } r > a, \end{cases} \quad (14c)$$

as shown Figure 1. For these profiles, we consider the dimensionless parameters:  $\beta_0 = -16.42$ ,  $\beta_1 = 20.30$ ,  $q_0 = 1.0$  and  $q_a = 4.0$ ; and, before carrying out the adimensionalization, the parameters:  $v_0 = -5.98$  km/s,

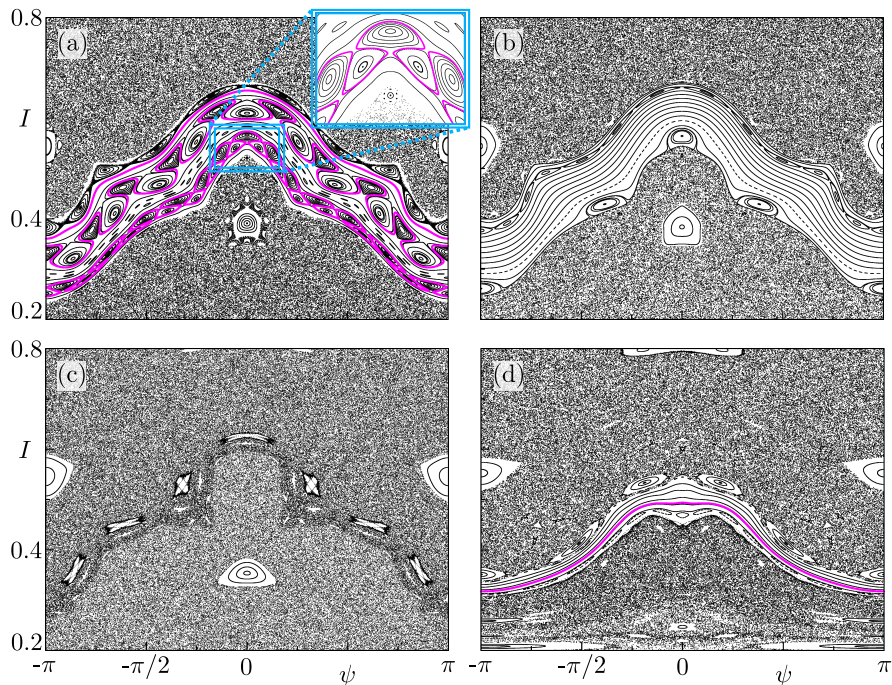


FIG. 5. Poincaré sections for  $\phi_1 = 2.283 \times 10^{-2}$  and (a)  $\rho = 0.0$ , (b)  $\rho = 1.637 \times 10^{-2}$ , (c)  $\rho = 3.770 \times 10^{-2}$  and (d)  $\rho = 5.556 \times 10^{-2}$ . Shearless transport barriers are colored in magenta.

$v_1 = 11.793$  km/s,  $E_0 = -6.0$  kV/m,  $E_1 = 5.751$  kV/m and  $E_2 = -2.592$  kV/m, i.e.,  $E_a = 2.274$  kV/m. Furthermore, for the electrostatic potential perturbation, we employ as dominant spatial modes,  $M = 16$  and  $L = 3$ , and as fundamental angular frequency  $\omega_0 = 60.0$  rad/ms (approximately 5.70 rad after the adimensionalization).

As a result, for the integrable case, non-monotonic behavior in the rotation number profile is obtained, see Figure 2, and, consequently, a STB is expected to exist. We show in the right panel of the figure a magnification localized in the reversed-shear region, where a subtle difference in the profile can be observed by varying the Larmor radius. For this case, the shearless point position displacement and its rotation number vary slightly with  $\rho$ . Because of that, near the STB, some rational and irrational orbits are not accessible anymore, if compared with the former case  $\rho = 0$ .

Now, concerning  $H_1 \neq 0$  for the non-integrable scenario, four harmonics corresponding to the main resonances,  $n = 2, 3, 4$ , and the non-resonant mode,  $n = 1$ , according to Figure 2, are taken. For the resonant modes, we adopt the amplitudes 0.80 V, 1.50 V and 0.85 V, which become the dimensionless fixed parameters  $\phi_2 = 1.95 \times 10^{-3}$ ,  $\phi_3 = 3.66 \times 10^{-3}$  and  $\phi_4 = 2.08 \times 10^{-3}$ , respectively. Additionally, we regard the amplitude  $\phi_1$ , which corresponds to the non-resonant mode, as a control parameter. Some studies have shown that the STB can be repeatedly destroyed and restored as the amplitude of this mode changes<sup>21</sup>.

Thus, for the scenario  $\phi_1 = 0$  shown in Figure 3, the impact of the FLR effect is illustrated. The left panel pro-

vides an overview of the Poincaré section for the massless case, where most of the KAM tori are broken. Only the non-twist barrier, formed by the STB (colored in black) and the neighboring invariant curves, survives. The effect of introducing the FLR is shown in the panels (b) and (c). Panel (b) presents a magnification of the STB region, while panel (c) shows some islands. The orbits in gray and black, which correspond to  $\rho = 0$ , are included as background and reference.

The barrier in Figure 3(b) exhibits minimal variation with  $\rho$ , except for a radial displacement and a subtle difference in shape. This can also be verified by looking at the rotation number profile in Figure 4(a). For this perturbation scenario, most differences are evidenced by looking at the islands. For example, as  $\rho$  increases, in panel 3(c.1), the center of the main island, close to  $I = 1.0$ , shifts; in panel 3(c.2), a local bifurcation occurs for the periodic orbits near  $I = 0.6$ ; and, in panel 3(c.3), new island chains appear in the lower chaotic region for the largest value considered of  $\rho$ . Also, a variation in the size of the islands can be observed.

When we increase the value of  $\phi_1$ , in contrast to the previous results, various transport barrier scenarios are obtained by varying  $\rho$ . This is depicted in the Poincaré sections of Figure 5 for  $\phi_1 = 2.283 \times 10^{-2}$ . In these scenarios, we observe that a bifurcation of the shearless curve occurs for the massless approximation, leading to the appearance of three different shearless transport barriers, see panel (a). This bifurcation can emerge due to cubic and quartic contributions in non-twist maps<sup>41,48</sup>. Then, introducing the FLR effect, panels (b) and (c),

the STBs disappear, leaving invariant curves and a partial barrier with sticky behavior, respectively. Eventually, a single shearless curve arises again when increasing the FLR until  $\rho = 5.556 \times 10^{-2}$ , as shown in (d). The rotation number profiles of the previous cases are shown in Figure 4(b) and 4(c); only for  $\rho = 3.770 \times 10^{-2}$ , there is no profile because all KAM tori are broken.

To get an overall view of how  $\phi_1$  affects the existence of shearless curves under different scenarios of  $\rho$ , we construct STB bifurcation diagrams as shown in Figure 6. For clarity, panel (a) includes only the massless case (black) and the  $\rho = 1.637 \times 10^{-2}$  case (red), while panel (b) shows scenarios for  $\rho = 3.770 \times 10^{-2}$  (green) and  $\rho = 5.556 \times 10^{-2}$  (blue). Fundamentally, for each value of  $\phi_1$ , we compute the rotation number profile and examine it to identify the presence of extreme points. If they are found, we plot points corresponding to the rotation numbers,  $\Omega_{\text{STB}}$ , of the shearless orbits.

Particularly for the parameters and profiles we have chosen, zonal flow bifurcations are inhibited as the FLR effect increases. They are common for large non-resonant perturbation amplitudes, for which cubic and quartic contributions appear to gain relevance in the numerical map. Furthermore, it is interesting to remark that the STB becomes more resilient to small and medium perturbations as  $\rho$  increases. This is clearly evidenced in panel (b), where the first two intervals of the barrier are larger and have almost no gaps compared to panel (a). In general, for the largest value of  $\rho$  considered, represented by the blue-colored bifurcation diagram, the barrier is broken up less frequently and restored more easily.

#### IV. CHAOTIC TRANSPORT REDUCTION

In this section, we explore additional diagnostics to gain broader insights into the influence of the FLR effect. We focus on chaotic transport's behavior as the control parameters vary, particularly after the non-twist barrier is broken.

So, we analyze the transmissivity,  $\eta_t$ , and the “transport current”,  $\nu_c$ , which are measurements compared to the probability of a given chaotic orbit escape from some region to another one and the escape rate, respectively. They are computed as follows:

- We select an ensemble of  $N$  randomly chosen initial conditions,  $\{\mathbf{z}_0^i\}_{i=1}^N$ , in a small chaotic area under the non-twist barrier. A previous survey of the phase space must be done to guarantee that by varying the parameters, the orbits are still in a chaotic region.
- We integrate each orbit until either a maximum of  $K$  iterations or it crosses the threshold  $I_\eta$ , i.e.,  $I_j^i > I_\eta$ . If the second criterion is fulfilled, we record the time  $K_c^i = j$ , and the orbit identified by  $\mathbf{z}_0^i$  is counted as an escaping orbit. Otherwise,  $K_c^i = 0$ . By doing this, we calculate a mean escape time

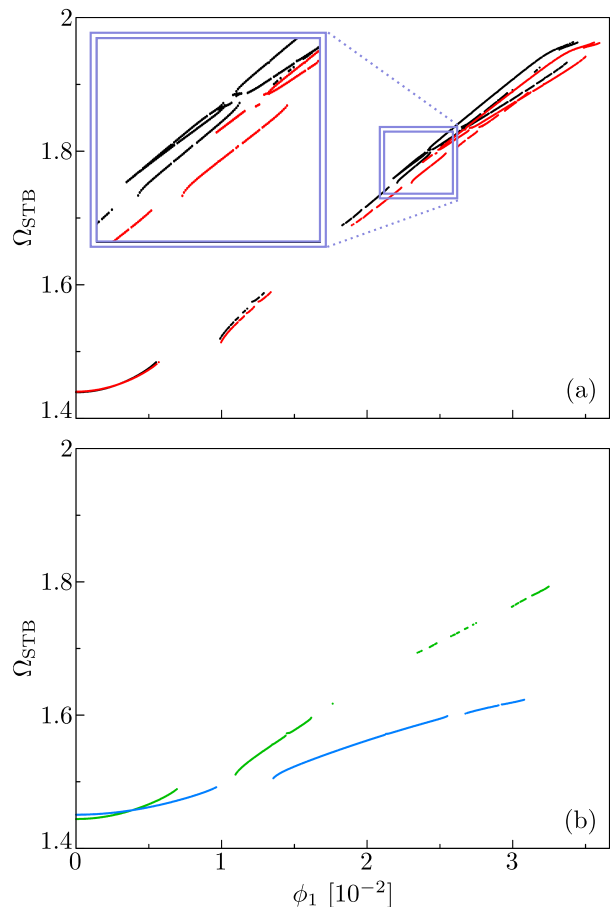


FIG. 6. Bifurcation diagrams of the shearless transport barrier for (a)  $\rho = 0$  (black) and  $\rho = 1.637 \times 10^{-2}$  (red), and for (b)  $\rho = 3.770 \times 10^{-2}$  (green) and  $\rho = 5.556 \times 10^{-2}$  (blue).

only considering the orbits that actually escape, as shown next.

- We compute the transmissivity as  $\eta_t = N_t/N$ , where  $N_t$  is the total number of escaping orbits, and the transport current as  $\nu_c = \eta_t / (\langle K_c \rangle / K)$ , where  $\langle K_c \rangle = \sum_{i=1}^N K_c^i / N_t$  is the mean escape time.

Notice that if  $\eta_t > 0$ , at least one orbit of the ensemble escapes; therefore, the non-twist barrier does not exist. Conversely, if  $\eta_t = 0$ , it is very likely that at least one KAM torus survives and acts as a barrier to transport. A small transmissivity indicates resistance to transport, such as sticky behavior or remnants of the non-twist barrier, as shown in Figure 5(c). This resistance prevents a fraction of the particles from crossing within the time period  $K$ . On the other hand, large values of  $\eta_t$  imply that the characteristic escape time of the particles is less than  $K$ .

However, equal  $\eta_t$  scenarios do not translate into equal chaotic transport conditions. This is because  $\langle K_c \rangle$  can vary significantly between scenarios. High transport situations occur when the transmissivity is large, and the

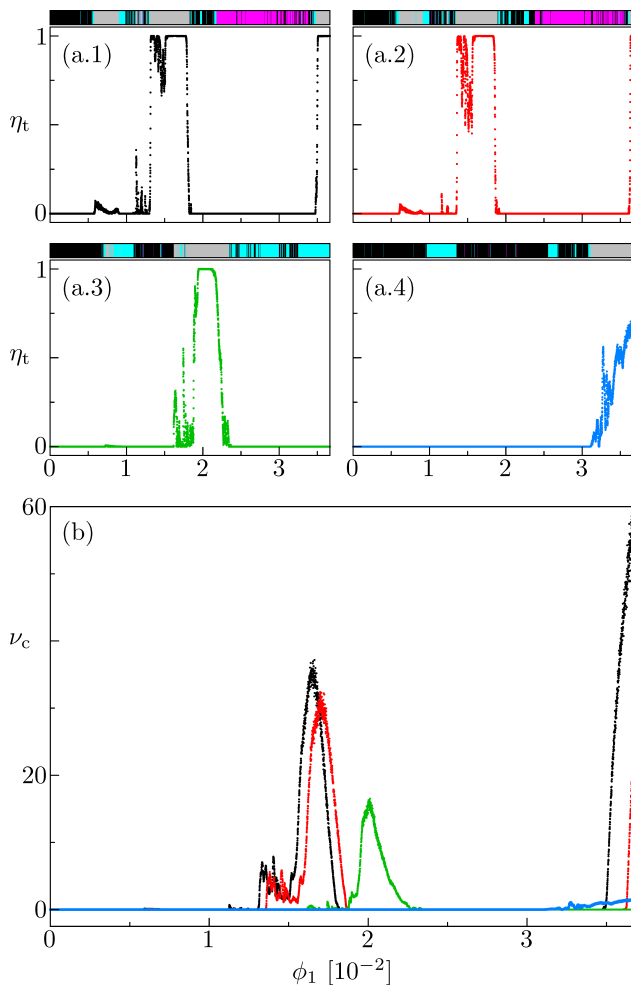


FIG. 7. Diagrams with  $\phi_1$  of the (a) transmissivity and (b) transport current for  $\rho = 0$  (black),  $\rho = 1.637 \times 10^{-2}$  (red),  $\rho = 3.770 \times 10^{-2}$  (green) and  $\rho = 5.556 \times 10^{-2}$  (blue). The color bars in the panels (a) represent the  $\phi_1$  intervals in which it was identified one shearless curve (black), two or more shearless curves (magenta), zero transmissivity but no STB (cyan), and  $\eta_t > 0$  (gray).

mean escape time is small, i.e., when the transport current  $\nu_c$  is large. Conversely, low transport occurs when the transport current is small, which corresponds to scenarios where  $\langle K_c \rangle$  is large, or  $\eta_t$  is small, or both.

In Figure 7, we present diagrams of the transmissivity and the transport current as a function of  $\phi_1$ . These diagrams were obtained using  $N = 10^3$  randomly chosen initial conditions in the intervals  $\psi_0 = [-0.54, -0.42]$  and  $I_0 = [0.275, 0.29]$ , integrated until either  $K = 5 \times 10^3$  crossings in the Poincaré section or until  $I_j^i > 0.8$ . Moreover, from the results in Figure 6, we identify intervals of  $\phi_1$  where scenarios with or without shearless transport barriers occur. Combining these results, we provide a detailed picture of the control of chaotic transport for the four Larmor radius values considered.

Then, from panel 7(a), we can say, for practical purposes, that there are similar behavior patterns in the first

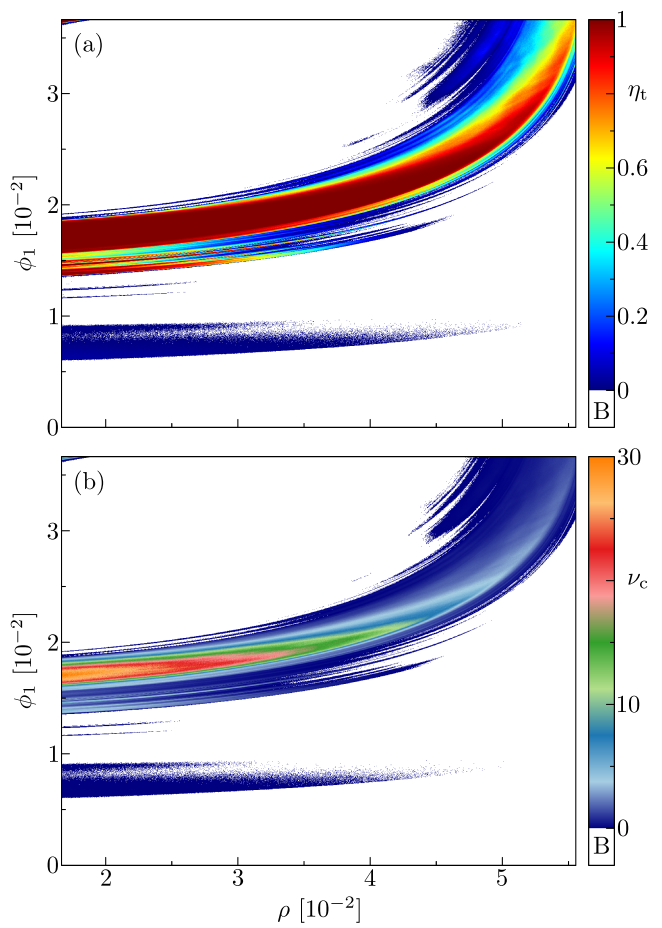


FIG. 8. Parameter spaces with  $\rho$  and  $\phi_1$ . Panel (a) shows the transmissivity,  $\eta_t$ , and panel (b) the current,  $\nu_c$ . The white color indicates, in both panels, that some type of barrier exists (B labeled scenario in the color bar).

three cases, except for a shift in the value of the perturbation at which maximum transmissivity occurs. In contrast, for the last case, the transmissivity never reaches the maximum value,  $\eta_t = 1$ , and increases more slowly with  $\phi_1$ . Of the four cases, this one is the most conclusive in terms of chaotic transport reduction through transmissivity diagnosis.

Additionally, as pointed out in the previous section, the color bars show that the STB typically bifurcates for small  $\rho$  values and large perturbations, and the first intervals of  $\phi_1$  are larger as  $\rho$  increases. Nonetheless, we now observe new intervals in which no STB exists, but different types of barriers inhibit chaotic transport, such as those in Figures 5(b) and 5(c). As shown in panels (a.3) and (a.4), these barriers appear more frequently for the largest values of  $\rho$ .

In panel 7(b), it becomes clearer that the FLR effect leads to a reduction in chaotic transport. As  $\rho$  increases, the transport current consistently decreases, with its peak shifting towards larger values of  $\phi_1$ . Furthermore, while the black, red, and green cases have a maximum transport current on the order of  $10^1$ , the blue

case reduces the transport current by one order of magnitude.

In a combined manner, the diagnoses of transmissivity and current transport allow us to discern subtle differences between scenarios. This is generally illustrated in the  $\rho \times \phi_1$  parameter spaces shown in Figure 8. There, scenarios with no chaotic transport are depicted in white, where STBs, KAM tori, or strong partial barriers may emerge. Conditions with low chaotic transport are predominantly shown in blue, indicative of partial barriers as well. Then, we observe that transport barriers tend to be more robust as the Larmor radius increases, requiring larger values of  $\phi_1$  to maximum transport. Moreover, following the main stripe, while we cannot observe significant variation in transmissivity, there is a clear systematic decrease in transport current conditions as  $\rho$  increases.

Finally, the lower stripe, which appears for most of the Larmor radius interval and within a perturbation interval for  $\phi_1$  of  $0.5 \times 10^{-2}$  to  $1 \times 10^{-2}$ , is linked to an interesting partial barrier dynamics, as detailed in Ref. 49. In these scenarios, even-period twin islands exhibit stable/unstable manifolds of the associated hyperbolic points that share a common branch which, in turn, separates two chaotic regions. Consequently, very few orbits manage to cross.

In conclusion, our findings suggest that the FLR effect plays a crucial role in promoting more robust transport barriers and reducing chaotic transport. Finally, we encourage other researchers to explore further aspects of this work, particularly the influence of the radial equilibrium electric field profile in chaotic transport and the symplectic map developed in Section II.

## V. CONCLUSIONS

A test particle guiding-center model has been implemented to evaluate the influence of the Larmor radius on chaotic transport and the onset of transport barriers in tokamaks. Specifically, we examined the guiding-center motion of a test particle as it moves along the magnetic field lines and is drifted by a gyro-averaged velocity caused by a non-uniform electrostatic field. The numerical simulations presented in this work were performed using parameters and plasma radial profiles for the tokamak TCABR; nonetheless, the results are valid for a wide class of toroidal machines.

By considering monotonic radial profiles of the safety factor and the plasma parallel velocity, along with an electric field composed of a radial equilibrium part with a non-monotonic profile, the twist condition of the dynamical system was violated. The plasma equilibria were perturbed by the superposition of electrostatic harmonic waves, and shearless transport barriers were observed to inhibit chaotic transport. Partial barriers and KAM tori were also found, contributing to the chaotic transport reduction.

We observed that, in general, transport barriers become more resilient to perturbations as the Larmor radius increases. With a large Larmor radius, transport barriers are destroyed only with high perturbation amplitudes. Furthermore, even in the absence of barriers, we found that the Larmor radius effect also reduces chaotic transport by making the orbits typically spend more time to escape and reducing the fraction of escaping orbits.

In particular, we have explored the behavior of transport barriers and chaotic transport by examining bifurcation diagrams of shearless transport barriers and the escape rate of an ensemble of chaotic orbits. We analyzed the influence of the electrostatic perturbation amplitude and the impact of the Larmor radius. Regarding the bifurcation diagrams, while varying the control parameters, we examined the rotation number profiles and identified the existence of extreme values where shearless transport barriers can be detected. For the escape rate, we computed the fraction of orbits able to escape from one region to another and the mean escape time of these orbits.

Our results indicate that for small Larmor radii, bifurcations of the shearless curve are likely to occur at high perturbation values, leading to the observation of multiple shearless barriers. However, as the Larmor radius increases, these bifurcations are mitigated. Additionally, we identified intervals of zero escape rate where no shearless transport barriers were found, meaning that other types of barriers emerge to inhibit chaotic transport, such as KAM tori and strong partial barriers. As the Larmor radius increases, the intervals of the electrostatic perturbation amplitude for which some transport barrier exists become greater. In particular, the hardest-to-break and easiest-to-restore shearless transport barriers were found at the largest Larmor radius examined.

We also discussed some chaotic transport diagnoses and showed that although the transmissivity, which measures the probability of a given chaotic orbit escaping, is a good indicator for characterizing transport, equal transmissivity scenarios do not necessarily translate into equal chaotic transport conditions due to differences in the characteristic mean escape time. Nevertheless, by using the escape rate, we were able to distinguish subtle differences between scenarios. Specifically, we demonstrated that the escape rate decreases as the Larmor radius increases. We surveyed parameter spaces involving the electrostatic perturbation amplitude and the Larmor radius, computing both transmissivity and escape rate.

In conclusion, we have demonstrated that the Larmor radius effect plays a crucial role in the dynamics of chaotic transport and the formation of transport barriers in tokamaks. As the Larmor radius effect increases, we observe a reduction in chaotic transport and an increase in the robustness of transport barriers.

## ACKNOWLEDGMENTS

The authors thank the financial support from the São Paulo Research Foundation (FAPESP, Brazil) under grants Nos. 2018/03211-6 and 2020/01399-8; the Brazilian Federal Agency CNPq under grants Nos. 304616/2021-4, 403120/2021-7 and 301019/2019-3; and the Comité Français d'Évaluation de la Coopération Universitaire et Scientifique avec le Brésil (CAPES/COFECUB) under grant No. 88887.675569/2022-00.

The Centre de Calcul Intensif d'Aix-Marseille is acknowledged for granting access to its high-performance computing resources.

## DATA AVAILABILITY STATEMENT

The data that support the findings of this study are available from the corresponding author upon reasonable request.

- <sup>1</sup>A. Wootton, B. Carreras, H. Matsumoto, K. McGuire, W. Peebles, C. P. Ritz, P. Terry, and S. Zweben, *Physics of Fluids B: Plasma Physics* **2**, 2879 (1990).
- <sup>2</sup>L. C. Woods, *Theory of tokamak transport: new aspects for nuclear fusion reactor design* (John Wiley & Sons, Weinheim, 2006).
- <sup>3</sup>J. Conner and H. Wilson, *Plasma Physics and Controlled Fusion* **36**, 719 (1994).
- <sup>4</sup>B. A. Carreras, *IEEE Transactions on Plasma Science* **25**, 1281 (1997).
- <sup>5</sup>G. M. Zaslavsky, *Physics Reports* **371**, 461 (2002).
- <sup>6</sup>M. Vlad, F. Spineanu, and D. Nendreaan, in *Annual Report of the EURATOM-MEdC Association* (2009) p. 54.
- <sup>7</sup>S. Futatani, D. del Castillo-Negrete, X. Garbet, S. Benkadda, and N. Dubuit, *Physical Review Letters* **109**, 185005 (2012).
- <sup>8</sup>J. Misguich, J. Reuss, D. Constantinescu, G. Steinbrecher, M. Vlad, F. Spineanu, B. Weyssow, and R. Balescu, *Plasma Physics and Controlled Fusion* **44**, L29 (2002).
- <sup>9</sup>R. Balescu, *Aspects of anomalous transport in plasmas* (Institute of Physics Pub., Bristol and Philadelphia, 2005).
- <sup>10</sup>I. L. Caldas, R. L. Viana, C. V. Abud, J. C. D. d. Fonseca, Z. d. O. Guimarães Filho, T. Kroetz, F. A. Marcus, A. B. Schelin, J. Szezech, D. L. Toufen, *et al.*, *Plasma Physics and Controlled Fusion* **54**, 124035 (2012).
- <sup>11</sup>P. Morrison, *Physics of Plasmas* **7**, 2279 (2000).
- <sup>12</sup>D. del Castillo-Negrete, J. Greene, and P. Morrison, *Physica D: Nonlinear Phenomena* **91**, 1 (1996).
- <sup>13</sup>A. Wurm, A. Apte, K. Fuchss, and P. Morrison, *Chaos: An Interdisciplinary Journal of Nonlinear Science* **15**, 023108 (2005).
- <sup>14</sup>S. Shinohara and Y. Aizawa, *Progress of Theoretical Physics* **100**, 219 (1998).
- <sup>15</sup>J. Szezech, I. L. Caldas, S. Lopes, R. L. Viana, and P. Morrison, *Chaos* **19**, 043108 (2009).
- <sup>16</sup>J. Szezech Jr, I. L. Caldas, S. R. Lopes, P. Morrison, and R. L. Viana, *Physical Review E* **86**, 036206 (2012).
- <sup>17</sup>W. Horton, *Plasma Physics and Controlled Fusion* **27**, 937 (1985).
- <sup>18</sup>W. Horton, H.-B. Park, J.-M. Kwon, D. Strozzi, P. Morrison, and D.-I. Choi, *Physics of Plasmas* **5**, 3910 (1998).
- <sup>19</sup>L. Souza, M. Sales, M. Mugnaine, J. Szezech Jr, I. Caldas, and R. Viana, *Physical Review E* **109**, 015202 (2024).
- <sup>20</sup>G. Grime, M. Roberto, R. Viana, Y. Elskens, and I. Caldas, *Journal of Plasma Physics* **89**, 835890101 (2023).
- <sup>21</sup>L. A. Osorio-Quiroga, M. Roberto, I. Caldas, R. Viana, and Y. Elskens, *Fundamental Plasma Physics* **6**, 100023 (2023).
- <sup>22</sup>G. Manfredi and R. Dendy, *Physical Review Letters* **76**, 4360 (1996).
- <sup>23</sup>G. Manfredi and R. Dendy, *Physics of Plasmas* **4**, 628 (1997).
- <sup>24</sup>D. del Castillo-Negrete and J. Martinell, *Communications in Nonlinear Science and Numerical Simulation* **17**, 2031 (2012).
- <sup>25</sup>J. Da Fonseca, D. del Castillo-Negrete, and I. L. Caldas, *Physics of Plasmas* **21**, 092310 (2014).
- <sup>26</sup>M. Stanzani, F. Arlotti, G. Ciraolo, X. Garbet, and C. Chandre, arXiv preprint arXiv:2309.02461 (2023), forthcoming in *Physical Review E*.
- <sup>27</sup>J. da Fonseca, D. del Castillo-Negrete, I. M. Sokolov, and I. L. Caldas, *Physics of Plasmas* **23**, 082308 (2016).
- <sup>28</sup>N. Kryukov, J. J. Martinell, and D. del Castillo-Negrete, *Journal of Plasma Physics* **84**, 905840301 (2018).
- <sup>29</sup>R. D. Hazeltine and F. L. Waelbroeck, *The framework of plasma physics* (CRC Press, Boca Raton, Florida, 2018).
- <sup>30</sup>S. Annibaldi, G. Manfredi, and R. Dendy, *Physics of Plasmas* **9**, 791 (2002).
- <sup>31</sup>A. J. Lichtenberg and M. A. Lieberman, *Regular and chaotic dynamics*, Vol. 38 (Springer-Verlag, New York, 1992).
- <sup>32</sup>J. Howard and S. Høhs, *Physical Review A* **29**, 418 (1984).
- <sup>33</sup>K. Rosalem, M. Roberto, and I. L. Caldas, *Nuclear Fusion* **54**, 064001 (2014).
- <sup>34</sup>F. A. Marcus, M. Roberto, I. L. Caldas, K. Rosalem, and Y. Elskens, *Physics of Plasmas* **26**, 022302 (2019).
- <sup>35</sup>L. A. Osorio-Quiroga, G. C. Grime, M. Roberto, R. L. Viana, Y. Elskens, and I. L. Caldas, *Brazilian Journal of Physics* **53**, 96 (2023).
- <sup>36</sup>J. Kim, K. Burrell, P. Gohil, R. Groebner, Y.-B. Kim, H. S. John, R. Seraydarian, and M. Wade, *Physical Review Letters* **72**, 2199 (1994).
- <sup>37</sup>G. A. Oda and I. Caldas, *Chaos, Solitons & Fractals* **5**, 15 (1995).
- <sup>38</sup>D. del Castillo-Negrete and P. Morrison, *Physics of Fluids A: Fluid Dynamics* **5**, 948 (1993).
- <sup>39</sup>R. Balescu, *Physical Review E* **58**, 3781 (1998).
- <sup>40</sup>R. P. Behringer, S. D. Meyers, and H. L. Swinney, *Physics of Fluids A: Fluid Dynamics* **3**, 1243 (1991).
- <sup>41</sup>J. E. Howard and J. Humpherys, *Physica D: Nonlinear Phenomena* **80**, 256 (1995).
- <sup>42</sup>S. Shinohara and Y. Aizawa, *Progress of Theoretical Physics* **97**, 379 (1997).
- <sup>43</sup>G. Engeln-Müllges and F. Uhlig, *Numerical algorithms with C* (Springer Science & Business Media, Berlin, 1996).
- <sup>44</sup>S. Das and J. A. Yorke, *Nonlinearity* **31**, 491 (2018).
- <sup>45</sup>F. A. Marcus, I. L. Caldas, Z. d. O. Guimarães-Filho, P. J. Morrison, W. Horton, Y. K. Kuznetsov, and I. C. Nascimento, *Physics of Plasmas* **15** (2008).
- <sup>46</sup>J. H. F. Severo, I. C. Nascimento, Y. K. Kuznetsov, R. M. O. Galvão, Z. d. O. Guimarães-Filho, F. Borges, O. Usuriaga, J. I. Elizondo, W. De Sá, E. K. Sanada, *et al.*, *Nuclear Fusion* **49**, 115026 (2009).
- <sup>47</sup>R. Galvão, C. Amador, W. Baquero, F. Borges, I. L. Caldas, N. Cuevas, V. Duarte, A. Elfimov, J. Elizondo, A. Fonseca, *et al.*, in *Journal of Physics: Conference Series*, Vol. 591 (IOP Publishing, 2015) p. 012001.
- <sup>48</sup>G. C. Grime, M. Roberto, R. L. Viana, Y. Elskens, and I. L. Caldas, *Chaos, Solitons & Fractals* **169**, 113231 (2023).
- <sup>49</sup>M. Mugnaine, J. Szezech Jr, R. Viana, I. Caldas, and P. Morrison, arXiv preprint arXiv:2406.19947 (2024).